

Precision Covalent Organic Frameworks for Surface Nucleation Control

Vikramjeet Singh, Jianhui Zhang, Jianan Chen, Christoph G. Salzmann, and Manish K. Tiwari*

Unwanted accumulation of ice and lime scale crystals on surfaces is a long-standing challenge with major economic and sustainability implications. Passive inhibition of icing and scaling by liquid-repellent surfaces are often inadequate, susceptible to surface failure under harsh conditions, and unsuitable for long-term/real-life usages. Such surfaces often require a multiplicity of additional features such as optical transparency, robust impact resistance, and ability to prevent contamination from low surface energy liquids. Unfortunately, most promising advances have relied on using perfluoro compounds, which are bio-persistent and/or highly toxic. Here it is shown that organic, reticular mesoporous structures, covalent organic frameworks (COFs), may offer a solution. By exploiting simple and scalable synthesis of defect-free COFs and rational post-synthetic functionalization, nanocoatings with precision nanoporosity (morphology) are prepared that can inhibit nucleation at the molecular level without compromising the related contamination prevention and robustness. The results offer a simple strategy to exploit the nanoconfinement effect, which remarkably delays the nucleation of ice and scale formation on surfaces. Ice nucleation is suppressed down to $-28\text{ }^{\circ}\text{C}$, scale formation is avoided for >2 weeks in supersaturated conditions, and jets of organic solvents impacting at Weber numbers $>10^5$ are resisted with surfaces that also offer optical transparency ($>92\%$).

1. Introduction


Controlling undesirable nucleation is an issue of broad implications, especially in the case of scaling and icing.^[1–4] Preventing/delaying scaling of calcium carbonate (CaCO_3) on surfaces is a challenge, with a major impact in a diversity of applications, such as heat exchangers, oil and gas extraction, water treatment systems,^[3,5] etc. Scaling of CaCO_3 on pipelines adds to the high energy consumption and dangerous microbial growth. There are several active and passive scale inhibition methods, such as mechanical cleaning, acid-base cleaning, and the addition of scale inhibitors (phosphates and polymeric) that are being practiced at the commercial level.^[6,7] However, they are either expensive and/or inefficient and, often, pose a direct threat to the environment by releasing hazardous chemicals.^[8] Despite extensive efforts to understand the effect of ions, pH, temperature, medium flow rate, impurities, suspended solids, substrate materials, and surface physicochemical properties on the nucleation and crystal growth of CaCO_3 , the mechanisms of scaling remain

unresolved.^[3] For example, Zhao et al.^[9] showed that thin hydrophobic polymer coating significantly reduced the heterogeneous nucleation of CaCO_3 . However, these coatings often face durability challenges and are unsuited for conditions where other contaminants (e.g., microbes, dirt, oils, etc.) are present. Similar to scaling, undesirable ice formation on infrastructure and transport components (e.g., power lines, ground transport vehicles, aircrafts, etc.) can impair safety and may cause life-threatening accidents.^[10] Therefore, passive prevention of ice and scale formation on surfaces, by using liquid-repellent, superhydrophobic, and slippery liquid-infused surfaces has received due attention.^[11,12] However, such surface treatments mainly relied on the use of perfluoro compounds (PFCs) due to their lowest surface energy ($<10\text{ mN m}^{-1}$) among others, which has serious health and environmental concerns.^[13–15] Additionally, these surfaces tend to lose their non-wetting characteristics under harsh conditions and are not suitable for long-term use.^[16,17] Recent efforts to replace the PFCs with safer compounds and/or their decomposition into benign inorganic fluoride ions and oxygenated organic molecules explain the seriousness of the situation.^[14,18,19]

V. Singh, J. Zhang, M. K. Tiwari
Nanoengineered Systems Laboratory
UCL Mechanical Engineering
University College London
London WC1E 7JE, UK
E-mail: m.tiwari@ucl.ac.uk

V. Singh, J. Zhang, M. K. Tiwari
Wellcome/EPSCRC Centre for Interventional and Surgical Sciences
University College London
London W1W 7TS, UK

J. Chen, C. G. Salzmann
Department of Chemistry
University College London
20 Gordon Street, London WC1H 0AJ, UK

 The ORCID identification number(s) for the author(s) of this article can be found under <https://doi.org/10.1002/adma.202302466>

© 2023 The Authors. Advanced Materials published by Wiley-VCH GmbH. This is an open access article under the terms of the Creative Commons Attribution License, which permits use, distribution and reproduction in any medium, provided the original work is properly cited.

DOI: 10.1002/adma.202302466

Due to their high surface energy ($>20 \text{ mN m}^{-1}$), fluorine-free surfaces are susceptible to contamination from oils and low surface tension liquids which are commonplace in everyday usage. Strategies, such as re-entrant surface texture to achieve superoleophobicity are impractical due to their complicated design and low-impact resistance.^[20,21] Metal-organic framework (MOF) based, slippery nanohierarchical surfaces were recently introduced to overcome some of these problems.^[22] However, as well as their well-known structural brittleness, inorganic components in MOFs make them chemically susceptible.^[23]

Understanding nucleation and crystal growth mechanisms for ice and lime scales has motivated works on suitable surfaces.^[24–26] For example, Bai et al. investigated the critical nucleus size of ice formation and showed that beyond 8 nm size, the presence of graphene oxide sheets increased the nucleation temperature (T_{IN}) to $\approx 10 \text{ }^\circ\text{C}$.^[27] With substantial improvements in classic nucleation theory, some of us previously showed that surfaces with precise concave nanotexture can significantly suppress ice nucleation through the interface nanoconfinement effect^[28]; however, the issue of producing such surface treatments at scale is a major challenge. Fabrication of surfaces with mechanically robust nanotextures with a few-nanometer manufacturing precision is extremely challenging, even with compromising the scalability. The use of anti-freezing proteins is also an attractive approach, albeit somewhat limited by the highly susceptible nature of peptide linkages that degrade under mild acidic/basic conditions.^[29] Similarly, nucleation investigations on the formation of CaCO_3 in fine pores also indicate that nanoscale confinement may be a general strategy that also works for scale inhibition.^[30] Despite having a clear theoretical steer, potentially scalable strategies to make surfaces with $<10 \text{ nm}$ precise nanocavities remain a challenge. Therefore, to overcome these fundamental challenges, here we exploit surface-grown covalent organic frameworks (COFs) to inhibit the nucleation of ice and CaCO_3 (Figure 1A). In fact, the advances in classical nucleation theory suggest that the surface concave nanotexture smaller than the critical nucleus radii (often below 10 nm) could potentially inhibit the nucleation of ice and minerals.^[28,31] Therefore, $\text{O}(1) \text{ nm}$ -precise texture, which is naturally accessible through porous materials such as COFs, MOFs or graphene, etc., offers a tremendous opportunity to realize nanocoatings for nucleation prevention. Top-down nanofabrication approaches are limited in their ability to go to such high precision. Specifically, COFs have advantages over graphene and MOFs, being mechanochemically more robust and defect-free due to inherent structural characteristics.^[32,33] Therefore, in this work imine-linked COF, with 1.8 nm pores, is selected to apply as a simple nanocoating for surface nucleation control (Figure 1B). Scalable solid–vapor interfacial polymerization (SV-IP) of COFs and subsequent post-functionalization with silane (to reduce surface energy) is used to obtain surfaces that show excellent anti-icing and anti-scaling characteristics. Additionally, they feature optical transparency, amphiphobicity, mechanochemical robustness and, last but not least, resistance to impact by high-speed jets of water and low surface tension liquids, which should widen their usage—scaling issue is rarely encountered in isolation. We also avoid using any fluorine-based surface treatments in order to ensure the eco-friendly nature of the surface.

2. Surface Fabrication and Characterization

A simplified SV-IP method^[34] was used (Experimental Section) to grow COF film on different substrates, prefunctionalized with aminopropyltriethoxy silane (APTES) such as glass, copper, silicon and aluminum (Figures S1, S1B, Supporting Information). Within COFs, enamine-based COFs were selected due to their hydrolytic stability.^[35] The concentration of the organic linkers, 2, 4, 6-triformylphloroglucinol (TFP) and *p*-phenylenediamine (PDA) was tuned to maintain the transparency and mechanical robustness by controlling the thickness of the coating (Experimental Section). With an increase in the concentration of linkers from $2 \text{ mg}/10 \text{ mg}$ (TFP/PDA, respectively) to $20 \text{ mg}/40 \text{ mg}$, the transparency of the surface went down significantly (Figure S2, Supporting Information). As synthesized COF coating was functionalized with trichloro-octadecylsilane to alter the surface wettability from hydrophilic to hydrophobic. Silane bonds to the hydroxyl functional groups presented on the COF linker through strong covalent linkage, that is, oxane bond. The reactant concentrations were systematically varied to obtain a surface that exhibited $\geq 90\%$ transmittance throughout the visible spectrum (Figure 1C; Figure S3, Supporting Information). The chemical structure of COFs was confirmed by FTIR (Figure S4, Supporting Information) with specific peaks at 1250 cm^{-1} for C–N stretching and 1695 cm^{-1} for C=C functional groups. Additionally, Raman spectroscopy of coated samples yielded peaks at 787 cm^{-1} (C–N) and 1605 cm^{-1} (C=O), confirming successful COF synthesis (Figure S5, Supporting Information). The COF crystallinity was confirmed by powder x-ray diffraction (Figure S6, Supporting Information), with specific diffraction peaks at $\approx 4.7^\circ$ (100 reflection plane), in agreement with the literature.^[36] The BET-specific surface area of the COF film was measured $\approx 55 \text{ m}^2$ using Krypton physisorption and the steadily increased adsorption (Figure S7, Supporting Information) at a relatively low-pressure range (<0.3) suggested the mesoporous structure of the material.^[37,38] The silane-treated surface was slippery (Figure 1D) with a water drop advancing contact angle (θ_{Adv}) $\approx 110^\circ$, the contact angle of hysteresis ($\Delta\theta$) $\approx 7^\circ$ and sliding angle $\approx 14^\circ$ (tested using $\approx 15 \mu\text{L}$ water droplet). Contrary to the control (bare glass) surface, carbon powder was easily removed by water drops sliding off the surface, confirming the self-cleaning characteristics (Figure S8, Movie S1, Supporting Information). The surface morphology imaged using a scanning electron microscope (SEM) is presented in Figure S9A–C (Supporting Information). A smooth surface with shallow roughness is observed at higher magnifications. The thickness of COF film, checked by imaging the cross-section under SEM, was $\approx 231 \text{ nm}$ (Figure 1E). The porous nature of the COF film was confirmed using a transmission electron microscope (TEM) (see Figure 1F). The film was scanned using TEM at multiple sites to confirm its defect-free characteristics (Figure S10, Supporting Information). The smooth topology of the COF coating was also confirmed using atomic force microscopy (AFM) (see Figure 1G; Figure S11, Supporting Information). 3D AFM image further confirmed the smoothness and the root-mean-square roughness (R_a) of the coating to be 4.5 nm (Figure 1G; Figure S11, Supporting Information). Height analysis by AFM confirmed the average coating thickness to be $\approx 300 \text{ nm}$ (Figure 1H,I).

The scalability potential of the method is shown by coating half of the $20 \text{ cm} \times 15 \text{ cm}$ glass substrate (Figure S12,

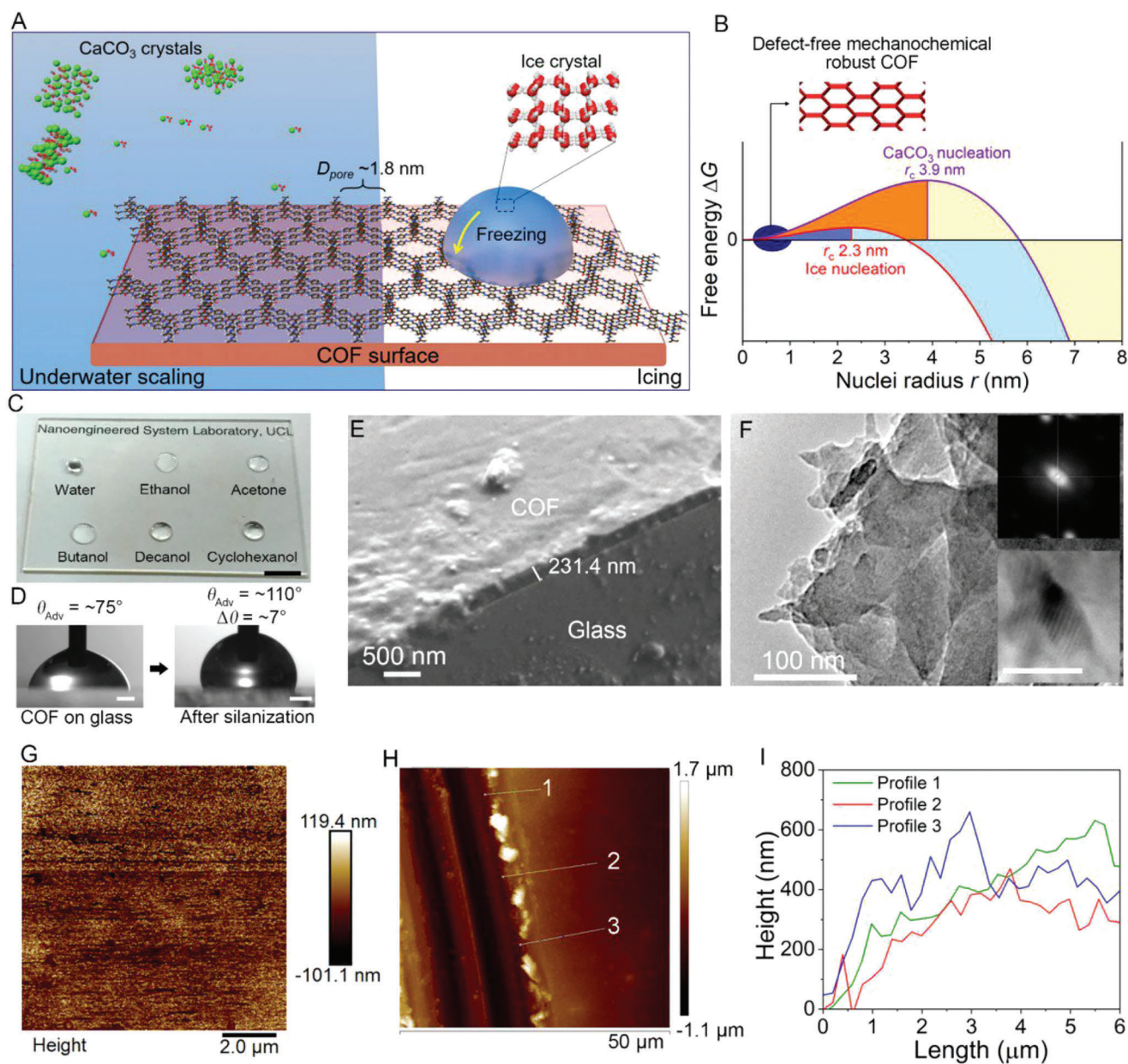


Figure 1. Rational nucleation inhibition strategy and schematic of smooth and amphiphobic surface grown COFs as a uniquely suited and potentially scalable nanocoating. A) Nucleation inhibition of ice and CaCO_3 on COF (pore diameter = 1.8 nm) surface. B) Free energy diagram showing critical nucleus radii of ice and CaCO_3 , confirming COF as a rational choice, with their defect-free growth and inherent mechanochemical robustness. C) Image showing droplets of water, ethanol, acetone, butanol, 1-decanol, and cyclohexanol on the transparent COF-coated glass substrate (scale bar = 1 cm). The amphiphobicity is achieved without any halogen chemistry. D) Advancing contact angle (θ_{Adv}) and contact angle hysteresis ($\Delta\theta$) for a water droplet on pristine COF on glass and after functionalization with trichlorooctadecyl silane (scale bar = 1 cm). E) Cross-section of COF coated on glass confirming nanometer thickness. F) TEM image showing the porous nature of the COF film. Inset showing electron diffraction pattern and the corresponding zoomed-in image. G) AFM image of the COF surface. H) AFM scan of scratched COF coating for height analysis and I) height profiles of the scratched section on a glass substrate.

Movie S2, Supporting Information). Half of the substrate was left uncoated for a clear presentation of the wettability difference. The functionalized COF surface offered a smooth amphiphobic surface on which water, vegetable oil, alcohols, and ketones slid off easily at $\leq 15^\circ$ angles (Movies S3, S4, Supporting Information). Furthermore, solvents such as butanone (23.9 mN m^{-1}), ethanol (22.1 mN m^{-1}), methanol (22.5 mN m^{-1}), acetone (25.2 mN m^{-1}),

1-butanol (25 mN m^{-1}), 1-decanol (28.5 mN m^{-1}), ethylene glycol (47 mN m^{-1}), cyclohexanol (33.4 mN m^{-1}) and 1,2-butanediol (37.2 mN m^{-1}) were tested and in each case, the corresponding droplet slid off at 15° inclination (Figure 2A; Figure S13, Supporting Information). Drop impacts at 1.4 and 4.2 m s^{-1} (drop diameter $\approx 2.7 \text{ mm}$), with relatively low and high impact kinetic energy offered the first insight into liquid impacts on the COF surfaces.

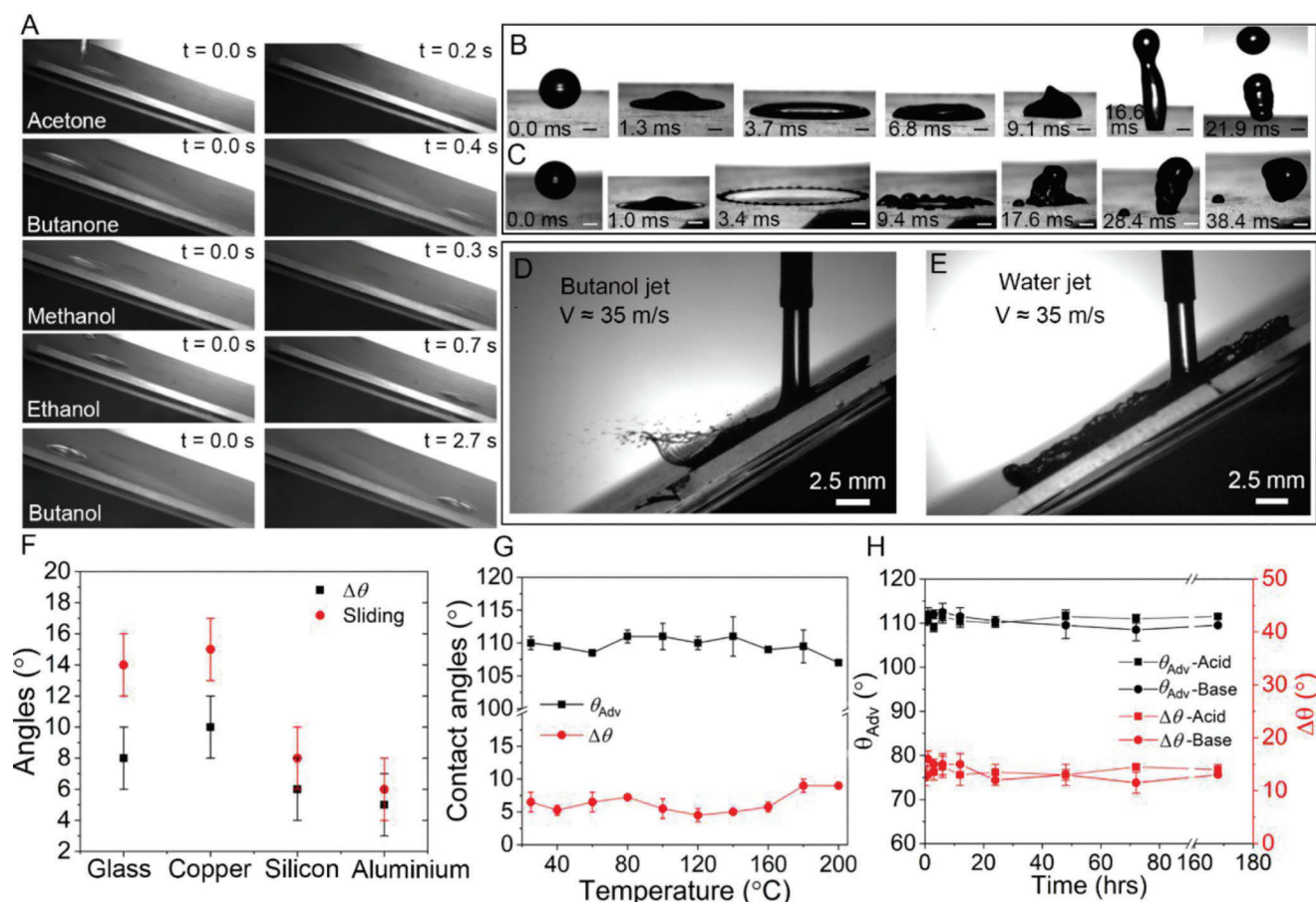


Figure 2. Amphiphobicity and robustness testing. A) Image sequence showing the sliding of low surface tension liquids at 15° tilt angles. The images are presented according to the drop speed (high to low from top to bottom). B) Time-lapse snapshots of drop impact on the COF surfaces at 1.4 m s⁻¹ and C) 4.2 m s⁻¹ impact velocities, respectively (scale = 2 mm). D) Butanol and E) water jets (nozzle diameter = 2.5 mm) impacting COF surfaces at ≈35 m s⁻¹. F) Sliding angles and $\Delta\theta$ on amphiphobic COF film coated on different substrates. G) Thermal stability test of the surface showing the change in $\Delta\theta$ and advancing angles of water droplets at a temperature range from 20 to 200 °C. H) Wetting angles (θ_{Adv} and $\Delta\theta$) representing the stability of COF coated on the glass surface in acid (pH = 1–2) and base (pH = 12–13) tested for one week.

The key stages in impact dynamics are shown in Figure 2B,C. A fraction of liquid detached from the droplet at a higher speed due to the hydrodynamic instability of the rim^[39] (Figure 2C). Next, high-speed jet impact tests were performed (see Figure 2D,E and the supplementary text). The surface resisted the water jet at the maximum speed attainable in our setup (≈35 m s⁻¹, liquid Weber number ≈42 500), even after repeated tests. We also tested the surface by impacting low surface tension liquids such as jets of ethanol and butanol tested at ≈35 m s⁻¹, resulting in liquid Weber number (We_l) calculated ≈109 300 and ≈99 200, respectively.^[40] The high-speed recordings for water, ethanol, and butanol jet impacts are presented in Movies S5–S7 (Supporting Information), respectively. After repeated jet impacts (three times), the water droplet sliding (Movie S8, Supporting Information) was repeated to confirm the retention of the slippery behavior of the coating. The effect of substrates' topology and composition was checked by measuring the $\Delta\theta$ and sliding angles for water droplets on different substrates coated with COFs (Figure 2F). The coating showed low $\Delta\theta$ ($\leq 10^\circ$) and sliding angles ($\leq 15^\circ$) on all the substrates, being lowest on aluminum (mirror finish). The thermal stability of COF coating was assessed by heating at a temperature

(20–200 °C) for 60 min followed by cooling down to room temperature and measuring the wetting angles. The surface maintained the slipperiness ($\Delta\theta \leq 10^\circ$) up to 200 °C (Figure 2G). The stability of the coating against corrosion was confirmed by immersing in strongly acidic (pH = 1–2) and basic media (pH = 12–13) for one week each (Figure 2H). Next, the mechanical robustness was tested using the standard tape-peel test. A high-tack tape (3M VHB™ S5952 with strong adhesive peel strength of 3900 N m⁻¹) was pressed on the surface with a 2-kg roller, before peeling off to complete one peel cycle (Figure S14, Supporting Information). No significant change was observed even after 50 repetitive cycles (Figure S15, Supporting Information). Following tape-peel, the surface was also tested using both drop impact (1.2 m s⁻¹) (Figure S16A, Supporting Information) and morphological characterization (Figure S16B, Supporting Information) to confirm the robustness.

3. Anti-icing

We evaluated the anti-icing capabilities of COF surface by measuring the delay in ice-nucleation in supercooled droplets and

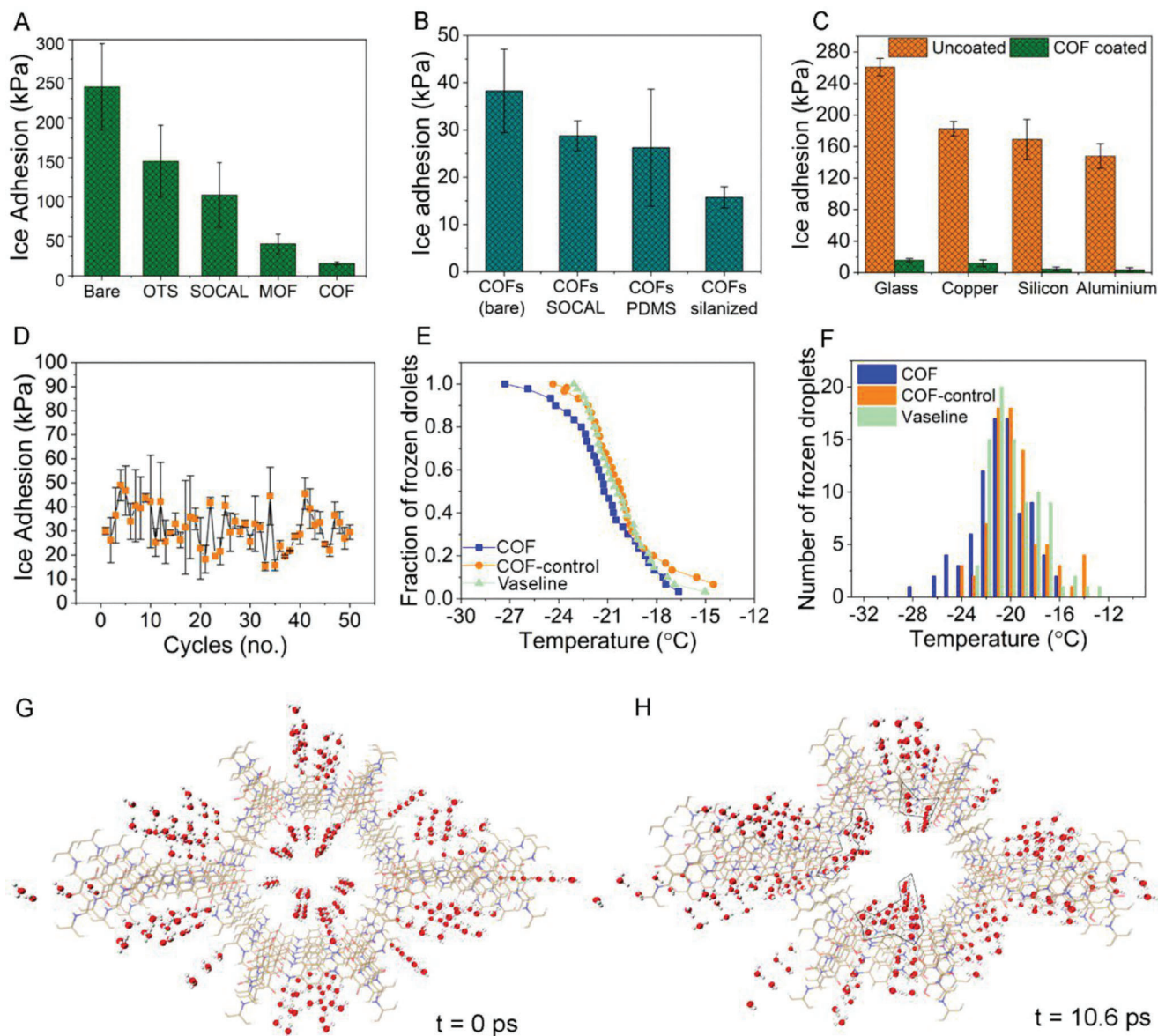


Figure 3. Anti-icing performance of the COF coating. A) Droplet freezing delay test showing a fraction of droplets frozen against temperature range comparing functionalized COF surface with unfunctionalized COFs (COF-control) and Vaseline petroleum jelly and B) histogram showing the number of droplets frozen against temperature on three different surfaces including Vaseline as a control. Data plotted here are the average of the three measurements. C) Ice adhesion strength of different treatments on glass substrate including bare glass as a control, glass functionalized with trichlorooctadecyl silane (OTS), ultra-smooth surface based on polydimethylsiloxane oligomers^[44] (SOCAL), our previously published nanohierarchical MOF surface^[22], and silane functionalized COF surfaces. D) Change in ice adhesion strength on bare COFs (without functionalization) and COFs with different functionalization, with flexible SOCAL, PDMS polymer, and long alkyl chains (trichloro-octadecylsilane). E) Ice adhesion strength comparison on glass, metals (copper and aluminum), and silicon substrates before and after being coated with COFs functionalized with silane. F) Unchanged ice adhesion strength on COF surface for 50 repeated icing/de-icing cycles. G) Top-view snapshot from the AIMD simulation taken at the start ($t = 0$ ps) and H) at the end (10.6 ps) showing the distortion of arranged water molecules due to high affinity toward the wall (hydrophilic functional groups) of COF pore.

ice-adhesion (supplementary text). The experimental details for the droplet freezing delay measurement are presented in Experimental Section. Vaseline petroleum jelly was used as a control due to its well-known inertness toward ice-nucleation^[41] and compared against functionalized COF coated on a glass substrate (Figure 3A). Clearly, the COFs are excellent in suppressing ice-nucleation, with the last few droplets freezing at ≈ -28 °C as op-

posed to ≈ -23 °C on Vaseline. Furthermore, unfunctionalized COF surfaces (without silane functionalization) were also tested and are compared in Figure 3B to check the impact of silane (hydrophobicity) on ice-nucleation. An almost similar freezing trend was observed on both the surfaces, unfunctionalized COFs and Vaseline, possibly due to perfectly arranged small nanopores which are akin to nanocavities reported elsewhere.^[28] Ice

adhesion test results are shown in Figure 3C–F. The adhesion on our functionalized COF films is compared against the bare glass and various nanoscale thick coatings such as a bare glass functionalized with trichloro-octadecyl silane (referred to as OTS), covalently attached dimethyl siloxane oligomer chains (SOCAL) and recently reported amphiphobic MOF^[22] (Figure 3C). The lowest ice adhesion strength of 15 ± 5 kPa was recorded on the COF coated on a glass substrate (Figure 3C) which is comparable to the value obtained on lubricant-infused slippery surfaces.^[42,43] In terms of functionalization, trichlorooctadecyl silane functionalized COFs showed the lowest ice adhesion, possibly due to the greater flexibility and larger chain length when compared to SOCAL oligomers which are relatively shorter in length (Figure 3D).^[44] Figure 3E compares the substrates and the decrease in ice adhesion strength is quite clear in each case. The surface robustness was also tested by repeating icing/de-icing cycles on a COF-coated glass substrate; within experimental repeatability error, no change in the ice adhesion strength was observed after 50 icing/de-icing cycles (Figure 3F). Following these cyclic assessments, the surface showed no sign of mechanical damage (see SEM in Figure S17, Supporting Information). The nucleation theory investigations (Supplementary text) point to the potential anti-icing mechanism of the COF surface through nanoconfinement effect. The critical nucleus radius to overcome the free energy barrier during ice crystal growth was calculated as ≈ 2.3 nm at -20 °C (Figure 1B), much larger than the radius of the COF pore (0.9 nm). Furthermore, molecular dynamics simulations based on first-principles potentials were used to study the arrangements of water molecules inside the COF pore and on the surface. The spatial distributions of water molecules inside the COF pore at the start (0 ps) and the end of simulations (10.6 ps) are shown in Figure 3G,H. At the end of the simulation, the water molecules were attracted to the wall, resulting in the deformation of the arrangements. The strong attraction of the water molecules toward the COF pore walls, evident through an increase in distance from the center (Figure S18, Supporting Information), suggests that the formation of ice nuclei and hydrogen bonding is hindered through the immobilization of water.^[45] Additionally, the structure of the water molecules, starting as a hexagonal ice crystal phase (denoted as I_h , i.e., ordinary ice or frozen water), was also investigated on the surface of the COF layer. The arrangements of the water molecules were observed to be distorted because of the strong interaction between the COF linker and the molecules of the ice basal plane, resulting in the lattice mismatch between the COF and ice crystals (Figure S19D, Supporting Information). This lattice mismatch and deflection help explain the observed increase in intermolecular distances and the formation of an interfacial quasi-liquid layer (Figure S19, Supporting Information). From an experimental perspective, this supports/explains the low ice adhesion strength measured on the COF surface.^[46,47]

4. Anti-scaling

To assess CaCO_3 scale nucleation inhibition, the COF coated, and uncoated glass and aluminum substrates were immersed in the supersaturated solution of calcium chloride (CaCl_2) and sodium bicarbonate (NaHCO_3)^[48] at 25 °C (Experimental Section). Glass substrate functionalized with trichloro-octadecylsilane (control)

was also evaluated to clarify the role of COFs. The growth of CaCO_3 was tracked using microscopy and the samples were carefully examined at 2-week intervals (Figure S20, Supporting Information). For the quantification, high-resolution images of the samples were recorded using SEM (Figure 4A,B; Figure S21, Supporting Information) and a 3D microscope (VHX-6000 series). The obtained images were processed in ImageJ software to calculate the total surface area covered with CaCO_3 crystals. The calculated data are presented in Figure 4C. The COF-coated surfaces performed exceptionally well in the prevention of CaCO_3 crystal growth; after two weeks only $\approx 0.5\%$ and $\approx 5\%$ for coated glass and aluminum substrates, respectively, were covered with CaCO_3 . The corresponding uncoated substrates had $\approx 85\%$ and $\approx 75\%$ coverage, respectively (see Figure 4C; Figure S22, Supporting Information). The silane functionalized hydrophobic glass (control) showed some resistance against crystal growth, with $\approx 38\%$ of the surface covered with CaCO_3 crystals after two weeks. The uncoated samples (Figure 4A; Figures S21,S22, Supporting Information) demonstrate thin patch-like depositions as well as large micrometer-sized crystals (20–50 μm) of CaCO_3 . The samples were mapped for elemental composition and distribution by energy dispersive spectroscopy (EDS) mapping. Deposited CaCO_3 was identified as the main source of Ca (Figure S23, Supporting Information). Other elements such as C, O, and Si, for glass substrates and additional Al for aluminum were also identified. High intensity of the Ca on control samples after two weeks confirmed the deposition of CaCO_3 , including large particles on both, glass and alumina substrates. In contrast, the intensity of Ca recorded on COF-coated samples was significantly lower, which confirms the exceptional anti-scaling performance of the COF coating. Inhibition of scaling on the half of a COF-coated glass substrate and large coverage of CaCO_3 on the uncoated half (Figure S24, Supporting Information) also highlight this. The nucleation inhibition for scales on the COF surface can be understood through nucleation theory (supplementary text, Figure S25, Supporting Information). The critical nucleus radius for CaCO_3 was calculated as 3.89 nm, which is much larger than the radius of the COF pore itself (0.9 nm). The results suggest that it is almost not possible for mineral ions to form stable nuclei inside the COF pores which might explain the experimental observations above.

5. Molecular Dynamics Study on CaCO_3 Nucleation Inhibition

Amorphous CaCO_3 is involved in the nucleation and growth of scales, and it usually follows a non-classical pathway.^[49] Born–Oppenheimer molecular dynamics simulation based on density functional theory was used^[50] to further understand the nucleation process inside COF pores from the non-classical perspective (Figure 4D, supplementary text). The 3D COF crystal structure was obtained from Cambridge Structural Database, followed by the addition of two CaCO_3 and two water molecules (Figure S26, Supporting Information).^[51,52] Formation of prenucleation clusters in the COF pores was studied at the atomistic level and two possible modes, monodentate (η^1) and bidentate (η^2) were considered based on the number of oxygen atoms coordinate with Ca^{2+} ion (Figure S28A,B, Supporting Information). A strong repulsion between Ca^{2+} and CO_3^{2-} ions was observed in the COF pore (Figure 4E), possibly due to nanoconfinement effect,^[53,54]

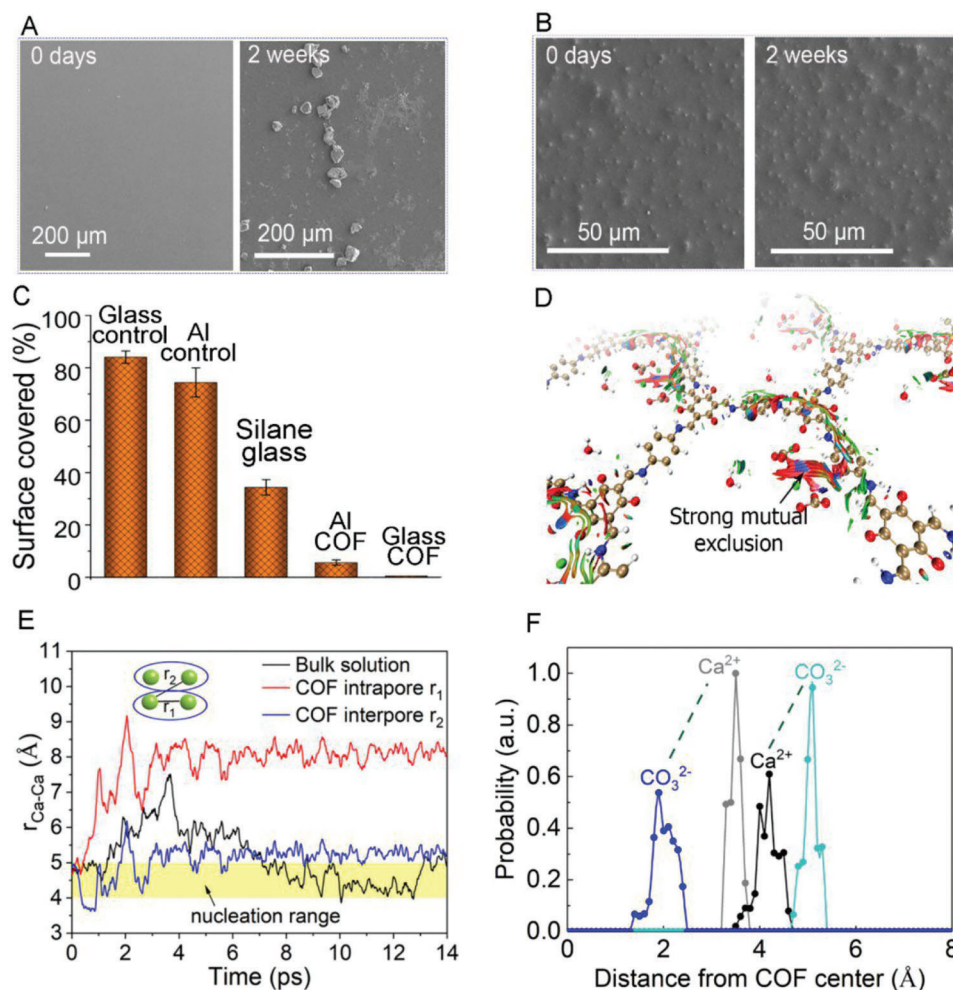


Figure 4. Scaling inhibition on COF-coated substrates. A) SEM images showing glass control and B) COF-coated glass before (0 days) and after (two weeks) immersion in the supersaturated solution of CaCl_2 and NaHCO_3 . C) The percentage of control and COF surfaces covered (on glass and aluminum substrates) with CaCO_3 deposition after two weeks of the scaling test. D) Strong mutual exclusion (repulsion) observed between Ca^{2+} and CO_3^{2-} ions in simulated COF pores and E) Evolution of distance between two Ca^{2+} ions $r_{\text{Ca-Ca}}$ over time in bulk and COF pores calculated in ab initio simulation. $r_{\text{Ca-Ca}}$ reduced to nucleation range in the bulk solution whereas, the Ca^{2+} ions remain well above the nucleation range due to strong repulsion in the COF pores. In schematic insets, the blue circles and green balls represent COF and Ca^{2+} ions, respectively. r_1 is the distance between two Ca^{2+} ions inside the same COF pore while r_2 is the longer distance between two Ca^{2+} ions in two adjacent COF pores. F) Probability of ions position from the center of the COF pore calculated using simulated data from 12.6 to 14 ps. The green dotted lines were used to connect the ionic pair.

whereas, ion pairs were observed to interact strongly via van der Waals forces in the bulk solution during ab initio simulation (Figure S28, Supporting Information). The time evolution of distance between two Ca^{2+} ions in bulk solution and COF pores, within a single pore (intra, r_1) and from an adjacent pore along a 2D channel (inter, r_2) was studied by comparing the nucleation range of a typical CaCO_3 crystal structure (Figure 4E). Ions in bulk solution start to form a nucleus after 7 ps, while, Ca^{2+} ions inside the COF pores remain separated, well above the nucleation range in both inter and intra pores, confirming strong repulsion. The time evolutions of the distances between Ca^{2+} and the oxygen (O_c) of the carbonate ions ($r_{\text{Ca-O}_c}$) in bulk solution and the COF pores are shown in Figure S28C,D (Supporting Information), respectively. $r_{\text{Ca-O}_c}$ of bulk solution shows a facile change between the two coordination modes of the ion pairs (η^1 and η^2), which is in agreement with previous reports.^[55] This association

mechanism is unstable thermodynamically, which helps in the formation of prenucleation amorphous CaCO_3 clusters by lowering the free energy barrier and increasing solvation entropy.^[49] Conversely, the coordination modes inside COF pores remain unchanged for over 14 ps, suggesting that the confinement of ions inside the COF pores might help in stabilizing the CaCO_3 monomer. The Gibbs free energy for the ion-pair reaction inside the COF pore was calculated around half of those in the bulk solution (see Table S1, Supporting Information), suggesting that the energy release and the rate constant is less in the case of COF pore than the bulk solution due to the nanoconfinement effect –resulting in nucleation inhibition process. Additionally, the hydration processes for both cases are shown in Figure S30 (Supporting Information). After equilibrium, the second hydration shells for both the calcium ions were occupied by oxygen from water molecules in the bulk solution, whereas the second

hydration shells for Ca^{2+} ions were empty in the COF pores. For closer insights into the nanoconfinement mechanism, the investigated spatial distribution and the position probabilities of the ion pairs inside the COF pore are shown in Figure S31A (Supporting Information) and Figure 4F, respectively. At the end of the dynamic simulation run, both the ions were pushed toward the wall of the COF pore due to the bigger size and their interaction with the functional groups (C=O) from the linker^[56] (Figure S31B, Supporting Information). This immobilization led to stable hydration shells –inhibiting the entropic solvent effect^[57] during the nucleation process in the COF pores. All these observations, including the strong mutual exclusion and stable coordination mode for the cation–anion pair in COF pores and the distance between the cation ions above the nucleation range, suggest that the COF pores with nanoscale precision should be highly efficient in inhibiting the nucleation of CaCO_3 , in agreement with our experiments.

In summary, we show that surface-grown COF films with post-synthetic alkylation offer exceptional properties as a thin and multifunctional coating due to their inherent precise nanoporous and robust structure. Fluorine-free functionalization of COFs with flexible alkyl chains enables the surface to resist the impacts of high-speed jets of low-surface tension liquids (such as ethanol and butanol). The study demonstrates that the miniature and precision COF pores (1.8 nm), can effectively inhibit the nucleation in both the cases, icing, and scaling. With the potentially scalable interfacial polymerization-based synthesis of defect-free surfaces, excellent anti-icing, and anti-scaling characteristics, the COF-based surface presented may elicit widespread usage.

6. Experimental Section

Materials: Glass slides (75 mm × 50 mm) were purchased from Thorlabs. Aluminum, copper, and silicon substrates were purchased from VWR International. All the chemicals including, *p*-phenylenediamine (PDA), octanoic acid, dimethyldimethoxysilane, sulfuric acid, polydimethylsiloxane, dimethyl formamide (DMF), glycol, glycerol, ethanol, acetone, isopropanol, 1-butanol, *n*-hexane, 1-decanol, butanone, 1-butanol, 1,4-butanediol, cyclohexaneol, benzene, toluene, chloroform, 3-aminopropyltriethoxy silane (APTES), calcium chloride (CaCl_2), sodium bicarbonate (Na_2HCO_3), trichloro-octadecyl silane, sodium hydroxide (NaOH) and hydrochloric acid (HCl) were purchased from Sigma Aldrich. Triformylphloroglucinol (TFP) was obtained from TCI chemicals. All the chemicals were used without further purification.

APTES Functionalization: The substrates (glass, copper, silicon, and aluminum) were pre-functionalized with APTES to obtain firmly attached and uniform COF film. In brief, a substrate was immersed into 1% of APTES in an *n*-hexane solution and incubated for 2 h at room temperature. The slides were thoroughly rinsed with *n*-hexane to remove the physisorbed APTES molecules and then dried under N_2 .

COF Film Synthesis via Solid–Vapor Interfacial Polymerization Method: COF film synthesis was adopted from literature with some modifications in the procedure to make it simpler by avoiding a spin coating step.^[34] Pre-functionalized substrates with APTES were placed horizontally in a glass petri dish on a hot plate at 80 °C. The solution of TFP in DMF (2 mg/10 mL) was spread onto the glass substrate with a pipette and covered with another petri dish for 2 h. Then the cover was removed to let it dry. In the second step, *p*-PDA was dissolved in octanoic acid (10 mg/20 mL) in a small glass container with round edges (100 mL) and placed in a big glass beaker of 1 L. The substrate was then placed on the container containing the PDA solution by directing the TFP layer downward (Figure S1B, Supporting Information). The beaker was sealed with aluminum foil and

placed in an oven at 150 °C for 12 h to allow solid–vapor interface polymerization. After completion of the polymerization reaction, the substrate was then extensively washed with chloroform and dried under vacuum at 80 °C for 12 h. The same process was used for the preparation of a larger sample to demonstrate the scalability of the process. A bespoke chamber made of steel (20 cm × 15 cm × 10 cm) was built for larger surface coating. The substrate was half-coated with COF by sealing half of the substrate using aluminum foil and adhesive tapes. The above-mentioned concentrations of organic linkers were tuned; a linker concentration of 2 mg/10 mL and 10 mg/10 mL for TFP and PDA, respectively resulted in the transparent coating with ≈300 nm thickness. A relatively thicker film was grown by using a high concentration of linkers (10 mg/40 mg for TFP/PDA) on a glass substrate for PXRD and BET characterizations. The growth time (12 h) and temperature (150 °C) were kept the same.

Post-Synthesis Functionalization of COFs with Silane: Alkyl silane (trichloro-octadecyl silane) was used to alter the wetting properties of the synthesized COF film. The liquid immersion method was adopted as used for APTES functionalization. The substrates (glass, copper, silicon, and aluminum) with COF film were immersed into 1% solution of trichloro-octadecyl silane in *n*-hexane for 2 h and placed at 120 °C for another 2 h for curing before rinsing with *n*-hexane. The hydrophobic and slippery substrate was then dried under the N_2 stream and used for further characterization.

Droplet Freezing Assay: Fraction-frozen curves were determined using a purpose-built closed setup containing a 30 × 30 mm aluminum substrate on top of a water-cooled Peltier element. A Feather 32u4 microcontroller from Adafruit was used to measure the temperature of the aluminum substrate (Pt100 sensor and MAX31865 module) and humidity inside the setup (AM2302 sensor). The substrate was either covered with a thin film of Vaseline petroleum jelly or COF-coated glass slides were attached with heat-conducting paste. A 5 × 5 array of 1 μL Milli-Q water droplets were pipetted on top of the surfaces at room temperature. To prevent frost-induced freezing of the droplets, the humidity inside the setup was kept below 5% with a flow of dry argon gas. The sample stage was cooled at 1 K min⁻¹ from room temperature to –30 °C using the PID algorithm in LabView on a PC which was connected to the microcontroller and a power supply for the Peltier element through USB. A movie of the cooling process was recorded with a USB camera to detect the individual freezing of the droplets.

Scaling Experiments: The scaling experiments were performed at static conditions at 25 °C. For the supersaturated CaCO_3 solution, a mixture of CaCl_2 (0.111 g, 1 mM) and Na_2HCO_3 (0.168 g, 2 mM) was stirred in 1 L of H_2O in a 2 L beaker to obtain a clear solution.^[48] Then the surfaces were immersed in the beaker in a tilted position along the beaker wall. Then the surfaces were characterized for crystal growth using a microscope (Leica, ICC50). The final samples were characterized using a 3D microscope (VHX-6000 series), SEM, and EDS for high-resolution images. The obtained images were processed with ImageJ for crystal growth quantification.

Supporting Information

Supporting Information is available from the Wiley Online Library or from the author.

Acknowledgements

The authors gratefully acknowledge funding from the European Union's Horizon 2020 Research and Innovation program under grant 801229 (HARMoNIC), European Research Council (ERC) grant 714712 (NICE-DROPS), and the Royal Society Wolfson Fellowship. J.Z. would like to acknowledge University College London's ORS and GRS Scholarships.

Conflict of Interest

The authors declare no conflict of interest.

Author Contributions

V.S. and M.K.T. conceived the research. V.S. and J.Z. performed the experiments collaboratively. J.Z. and J.C. led the simulations' work. C.G.S. facilitated the freezing delay experiments. M.K.T. supervised and managed the project. V.S. and J.Z. wrote the first draft of the manuscript followed by comments and revisions from all authors.

Data Availability Statement

The data that support the findings of this study are available in the supplementary material of this article.

Keywords

amphiphobic surfaces, anti-icing, anti-scaling, covalent organic frameworks, nucleation inhibition

Received: March 16, 2023

Revised: May 27, 2023

Published online:

- [1] J. D. Atkinson, B. J. Murray, M. T. Woodhouse, T. F. Whale, K. J. Baustian, K. S. Carslaw, S. Dobbie, D. O'sullivan, T. L. Malkin, *Nature* **2013**, 498, 355.
- [2] T. Kawasaki, H. Tanaka, *Proc. Natl. Acad. Sci. U. S. A.* **2010**, 107, 14036.
- [3] L. Lin, W. Jiang, X. Xu, P. Xu, *npj Clean Water* **2020**, 3, 25.
- [4] R. Demichelis, P. Raiteri, J. D. Gale, D. Quigley, D. Gebauer, *Nat. Commun.* **2011**, 2, 590.
- [5] F. Kohler, O. Pierre-Louis, D. K. Dysthe, *Nat. Commun.* **2022**, 13, 6990.
- [6] Z. Shen, J. Li, Ke Xu, L. Ding, H. Ren, *Desalination* **2012**, 284, 238.
- [7] R. G. M. d. A. Macedo, N. d. N. Marques, L. C. S. Paulucci, J. V. M. Cunha, M. A. Villetti, B. B. Castro, *Carbohydr. Polym.* **2019**, 215, 137.
- [8] A. Li, H. Zhang, Q. Liu, H. Zeng, *J. Colloid Interface Sci.* **2022**, 618, 507.
- [9] J. Zhao, M. Wang, M. S. Jebutu, M. Zhu, K. K. Gleason, *J. Mater. Chem. A* **2019**, 7, 17242.
- [10] S. Jung, M. K. Tiwari, N. V. Doan, D. Poulikakos, *Nat. Commun.* **2012**, 3, 615.
- [11] P. Kim, T. S. Wong, J. Alvarenga, M. J. Kreder, W. E. Adorno-Martinez, J. Aizenberg, *ACS Nano* **2012**, 6, 6569.
- [12] M. J. Kreder, J. Alvarenga, P. Kim, J. Aizenberg, *Nat. Rev. Mater.* **2016**, 1, 15003.
- [13] S. Shabanian, B. Khatir, A. Nisar, K. Golovin, *Nat. Sustain.* **2020**, 3, 1059.
- [14] B. Trang, Y. Li, X. S. Xue, M. Ateia, K. N. Houk, W. R. Dichtel, *Science* **2022**, 377, 839.
- [15] V. Jokinen, E. Kankuri, S. Hoshian, S. Franssila, R. H. A. Ras, *Adv. Mater.* **2018**, 30, 1705104.
- [16] S. Peppou-Chapman, J. K. Hong, A. Waterhouse, C. Neto, *Chem. Soc. Rev.* **2020**, 49, 3688.
- [17] J. Liu, Y. Sun, X. Zhou, X. Li, M. Kappl, W. Steffen, H. J. Butt, *Adv. Mater.* **2021**, 33, 2100237.
- [18] S. Joudan, R. J. Lundgren, *Science* **2022**, 377, 816.
- [19] S. K. Lahiri, Z. Azimi Dijvejin, K. Golovin, *Nat. Sustainability* **2023**, 6, 559.
- [20] A. Tuteja, W. Choi, M. Ma, J. M. Mabry, S. A. Mazzella, G. C. Rutledge, G. H. Mckinley, R. E. Cohen, *Science* **2007**, 318, 1618.
- [21] A. Tuteja, W. Choi, J. M. Mabry, G. H. Mckinley, R. E. Cohen, *Proc. Natl. Acad. Sci. U. S. A.* **2008**, 105, 18200.
- [22] V. Singh, X. Men, M. K. Tiwari, *Nano Lett.* **2021**, 21, 3480.
- [23] M. Kalaj, K. C. Bentz, S. Ayala, J. M. Palomba, K. S. Barcus, Y. Katayama, S. M. Cohen, *Chem. Rev.* **2020**, 120, 8267.
- [24] S. Dobberschütz, M. R. Nielsen, K. K. Sand, R. Civioc, N. Bovet, S. L. S. Stipp, M. P. Andersson, *Nat. Commun.* **2018**, 9, 1578.
- [25] H. Deng, S. Wang, X. Wang, C. Du, X. Shen, Y. Wang, F. Cui, *Regen. Biomater.* **2015**, 2, 187.
- [26] L. Salvati Manni, S. Assenza, M. Duss, J. J. Vallooran, F. Juranyi, S. Jurt, O. Zerbe, E. M. Landau, R. Mezzenga, *Nat. Nanotechnol.* **2019**, 14, 609.
- [27] G. Bai, D. Gao, Z. Liu, X. Zhou, J. Wang, *Nature* **2019**, 576, 437.
- [28] P. Eberle, M. K. Tiwari, T. Maitra, D. Poulikakos, *Nanoscale* **2014**, 6, 4874.
- [29] A. Eskandari, T. C. Leow, M. B. A. Rahman, S. N. Oslan, *Biomolecules* **2020**, 10, 1649.
- [30] M. Zeng, Yi-Y Kim, C. Anduix-Canto, C. Frontera, D. Laundry, N. Kapur, H. K. Christenson, F. C. Meldrum, *Proc. Natl. Acad. Sci. U. S. A.* **2018**, 115, 7670.
- [31] X. Zhou, Y. Sun, J. Liu, *Adv. Mater. Interfaces* **2021**, 8, 2100327.
- [32] M. Ding, X. Cai, H. L. Jiang, *Chem. Sci.* **2019**, 10, 10209.
- [33] A. P. Côté, A. I. Benin, N. W. Ockwig, M. O'keeffe, A. J. Matzger, O. M. Yaghi, *Science* **2005**, 310, 1166.
- [34] N. A. Khan, R. Zhang, H. Wu, J. Shen, J. Yuan, C. Fan, Li Cao, M. A. Olson, Z. Jiang, *J. Am. Chem. Soc.* **2020**, 142, 13450.
- [35] R. K. Sharma, P. Yadav, M. Yadav, R. Gupta, P. Rana, A. Srivastava, R. Zbořil, R. S. Varma, M. Antonietti, M. B. Gawande, *Mater. Horiz.* **2020**, 7, 411.
- [36] K. Dey, M. Pal, K. C. Rout, S. Kunjattu H, A. Das, R. Mukherjee, U. K. Kharul, R. Banerjee, *J. Am. Chem. Soc.* **2017**, 139, 13083.
- [37] D. Zilli, P. R. Bonelli, C. J. Gommès, S. Blacher, J.-P. Pirard, A. L. Cukierman, *Carbon* **2011**, 49, 980.
- [38] I. Stassen, M. Styles, G. Greci, H. V. Gorp, W. Vanderlinden, S. D. Feyter, P. Falcaro, D. D. Vos, P. Vereecken, R. Ameloot, *Nat. Mater.* **2016**, 15, 304.
- [39] A. L. Yarin, *Annu. Rev. Fluid Mech.* **2006**, 38, 159.
- [40] C. Peng, Z. Chen, M. K. Tiwari, *Nat. Mater.* **2018**, 17, 355.
- [41] M. Polen, T. Brubaker, J. Somers, R. C. Sullivan, *Atmos. Meas. Tech.* **2018**, 11, 5315.
- [42] A. Sandhu, O. J. Walker, A. Nistal, K. L. Choy, A. J. Clancy, *Chem. Commun.* **2019**, 55, 3215.
- [43] Bo Liu, K. Zhang, C. Tao, Y. Zhao, X. Li, K. Zhu, X. Yuan, *RSC Adv.* **2016**, 6, 70251.
- [44] L. Wang, T. J. McCarthy, *Angew. Chem., Int. Ed.* **2016**, 55, 244.
- [45] A. Hakimian, M. Mohebinia, M. Nazari, A. Davoodabadi, S. Nazifi, Z. Huang, J. Bao, H. Ghasemi, *Nat. Commun.* **2021**, 12, 6973.
- [46] S. Xiao, J. He, Z. Zhang, *Nanoscale* **2016**, 8, 14625.
- [47] Z. He, S. Xiao, H. Gao, J. He, Z. Zhang, *Soft Matter* **2017**, 13, 6562.
- [48] T. Zhang, Y. Wang, F. Zhang, X. Chen, G. Hu, J. Meng, S. Wang, *npj Asia Mater.* **2018**, 10, e471.
- [49] P. Raiteri, J. D. Gale, *J. Am. Chem. Soc.* **2010**, 132, 17623.
- [50] J. Hutter, M. Iannuzzi, F. Schiffmann, J. Vandevondele, *Wiley Interdiscip. Rev.: Comput. Mol. Sci.* **2014**, 4, 15.
- [51] B. P. Biswal, S. Kandambeth, S. Chandra, D. B. Shinde, S. Bera, S. Karak, B. Garai, U. K. Kharul, R. Banerjee, *J. Mater. Chem. A* **2015**, 3, 23664.
- [52] K. Zhang, Z. He, K. M. Gupta, J. Jiang, *Environ. Sci.: Water Res. Technol.* **2017**, 3, 735.
- [53] L. O. Hedges, S. Whitelam, *Soft Matter* **2012**, 8, 8624.
- [54] A. Katsman, I. Polishchuk, B. Pokroy, *Faraday Discuss.* **2022**, 235, 433.
- [55] D. D. Tommaso, N. H. De Leeuw, *J. Phys. Chem. B* **2008**, 112, 6965.
- [56] S. Goutham, A. Keerthi, A. Ismail, A. Bhardwaj, H. Jalali, Y. You, Y. Li, N. Hassani, H. Peng, M. V. S. Martins, F. C. Wang, M. Neek-Amal, B. Radha, *Nat. Nanotechnol.* **2023**, 18, 596.
- [57] D. Gebauer, A. Völkel, H. Cölfen, *Science* **2008**, 322, 1819.